

HBN-Encapsulated, Graphene-based, Room-temperature Terahertz Receivers, with High Speed and Low Noise

Leonardo Viti,* David G. Purdie, Antonio Lombardo, Andrea C. Ferrari, and Miriam S. Vitiello*



Cite This: *Nano Lett.* 2020, 20, 3169–3177



Read Online

ACCESS |

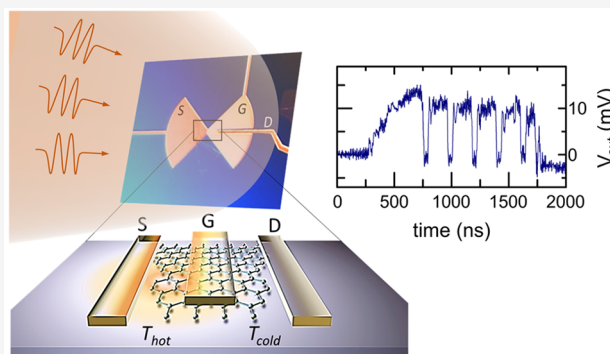
Metrics & More

Article Recommendations

Supporting Information

ABSTRACT: Uncooled terahertz photodetectors (PDs) showing fast (ps) response and high sensitivity (noise equivalent power (NEP) $< nW/Hz^{1/2}$) over a broad (0.5–10 THz) frequency range are needed for applications in high-resolution spectroscopy (relative accuracy $\sim 10^{-11}$), metrology, quantum information, security, imaging, optical communications. However, present terahertz receivers cannot provide the required balance between sensitivity, speed, operation temperature, and frequency range. Here, we demonstrate uncooled terahertz PDs combining the low ($\sim 2000 k_B \mu m^{-2}$) electronic specific heat of high mobility ($> 50\,000 cm^2 V^{-1} s^{-1}$) hexagonal boron nitride-encapsulated graphene, with asymmetric field enhancement produced by a bow-tie antenna, resonating at 3 THz. This produces a strong photo-thermoelectric conversion, which simultaneously leads to a combination of high sensitivity (NEP $\leq 160 pW Hz^{-1/2}$), fast response time ($\leq 3.3 ns$), and a 4 orders of magnitude dynamic range, making our devices the fastest, broad-band, low-noise, room-temperature terahertz PD, to date.

KEYWORDS: terahertz, photodetector, graphene, thermoelectric effect



Room-temperature (RT) detection, over the terahertz frequency range, is of great interest for a number of applications in biomedicine,^{1,2} security,³ spectroscopy,⁴ environmental monitoring⁵ real-time imaging,⁶ and high data-rate communications,⁷ as well as for unveiling fundamental properties of condensed matter systems at the nanoscale.^{8–10}

Many different RT detection technologies have been developed over the past two decades, with a largely variable range of sensitivities, response times (τ), operational frequency range, and underlying physical mechanisms.¹¹ Commercial RT terahertz sensors include thermal devices, such as pyroelectric¹¹ and Golay cells,¹¹ semiconductor-oxide¹² or metallic based microbolometers,¹ and solid-state electronic architectures, such as Schottky diodes¹³ and complementary metal–oxide semiconductor (CMOS)-based field effect transistors (FET).¹⁴

The sensitivity of a terahertz photodetector (PD) can be expressed in terms of its noise equivalent power (NEP), which indicates the minimum incident optical power required to achieve a unitary signal-to-noise ratio over a bandwidth of 1 Hz.¹⁵ Pyroelectric PDs have NEP $\sim 100 pW Hz^{-1/2}$,¹¹ $\tau \sim 10 ms$,¹¹ broadband operation over the range of 0.2–30 THz,¹¹ and are mostly single-pixel devices.⁶ Microbolometric terahertz cameras are the most common multipixel sensors.¹² They have broadband operation (0.2–100 THz),¹¹ low NEP $\sim 20 pW Hz^{-1/2}$,¹¹ but τ limited to $\sim 10–1000 \mu s$.¹¹ Solid-state electronic devices are significantly faster than these. For example, Schottky diodes have $\tau \geq 5 ps$ ¹⁶ with NEP $\sim 100 pW$

$Hz^{-1/2}$,¹⁶ but their performances rapidly decrease with operational frequency greater than 3 THz¹³ or when implemented in an array configuration.¹⁷ CMOS-based FETs are best suited for multipixel integration;¹⁸ broadband operation up to 9 THz with NEP $\sim 10 pW Hz^{-1/2}$ and with $\tau < 1 \mu s$ has been reported.^{19,20}

A promising route to combine the main advantages provided by the aforementioned technologies relies in the exploitation of layered materials (LMs). For these, the dominant detection mechanism can be tailored by design.²¹ Their ultrafast dynamics²² and the ease of fabrication^{23,24} and integration²⁵ can boost both the sensitivity and speed of terahertz PDs operating at RT. Single-layer graphene (SLG) and other LMs have been used to fabricate a variety of terahertz PDs.^{26–36} RT terahertz photodetection in a FET was demonstrated exploiting overdamped plasma waves (PW),^{14,37} photo-thermoelectric (PTE) rectification,^{33,36} bolometric detection,³⁸ or via a combination of the aforementioned phenomena.^{15,26,30,34,38}

Received: December 18, 2019

Revised: February 18, 2020

Published: April 17, 2020



The low ($\sim 100 \Omega$) channel and contact resistances in SLG FETs (GFETs) help in reducing the detector noise.³⁹ Contact resistance less than $100 \Omega \mu\text{m}$ can be obtained with edge contacts to encapsulated SLG in hexagonal boron nitride (hBN)⁴⁰ or with contact area cleaning and rapid thermal annealing.⁴¹ When terahertz rectification is mediated by the simultaneous modulation of carrier density (n) and drift velocity (v_d) in the channel, that is, in the PW-driven response, an increase in carrier mobility (μ) leads to a reduction of τ .⁴² This enables modulation frequencies $> 10 \text{ GHz}$ in the low-field limit (i.e., as long as velocity saturation effects can be neglected⁴²), since the maximum modulation frequency is expected to be proportional to μ .⁴²

SLG is also ideal for PTE PDs,^{36,43} owing to its gapless nature that allows broadband absorption from the UV to GHz frequencies.⁴⁴ The PTE effect entails a thermal gradient within the electronic distribution,⁴³ which yields the diffusion of carriers away from the hottest region.⁴⁴ In SLG, when electrons are heated by photon absorption, photogenerated carriers remain thermally decoupled from the crystal lattice.^{43,45} This is due to the difference between the electron–electron scattering time ($\sim 20 \text{ fs}$,^{22,46} needed for thermalization of the electronic distribution) and the slower ($\sim 2 \text{ ps}$ ^{43,46,47,53}) electron–phonon relaxation time. Therefore, a quasi-equilibrium state is reached, where the electronic temperature T_e is considerably higher than the lattice temperature T_L .⁴⁵ The electronic subsystem shows a low specific heat c_e ($\sim 2000 k_B \mu\text{m}^{-2}$ at 300 K , where k_B is the Boltzmann constant),^{48,49} which can lead to the ultrafast (50 fs) onset of thermal gradients^{49,50} and to a rapid overheating of the electronic distribution.⁴⁹ This is ideal for PTE-based devices, since all the absorbed electromagnetic energy is first transferred to electron heating, before being lost through other (slower) thermalization channels. Interaction with acoustic phonons occurs on a ps time scale.^{22,46,50,53} Therefore, the PTE conversion can be efficient, even though the Seebeck coefficient is relatively small ($S_b \sim 40 \mu\text{V K}^{-1}$) with respect to other LMs (e.g., black phosphorus³³). This is particularly effective at terahertz frequencies, because of the inhibition of ultrafast relaxation ($< 150 \text{ fs}$) via optical phonon emission by photoexcited electrons at energies $< 0.2 \text{ eV}$.^{22,46,52,53}

The small c_e stems from the density of states shrinking in proximity of the charge neutrality point (CNP) as a consequence of the linear band dispersion.⁴⁹ In particular, the analytical expression of the electronic specific heat c_e in proximity of the CNP (chemical potential $< k_B T$) is:⁴⁹ $c_e = 18\zeta(3)k_B^3 T_e^2 / (\pi(\hbar v_F)^2)$, where $\zeta(3) = 1.202$ is the zeta function, \hbar is the Planck constant, and $v_F = 1.1 \times 10^6 \text{ ms}^{-1}$ is the Fermi velocity. Therefore, c_e grows quadratically with T_e , reaching $\sim 2000 k_B \mu\text{m}^{-2}$ at 300 K .^{48,49} In contrast, the lattice specific heat (c_p) is more than 1000 times larger.⁴⁸ Hence, the combination of $c_e/c_p < 1000$ with $\mu > 50000 \text{ cm}^2 \text{ V}^{-1} \text{ s}^{-1}$ makes GFETs ideal for fast PTE terahertz PDs. Since SLG with $\mu > 70000 \text{ cm}^2 \text{ V}^{-1} \text{ s}^{-1}$ can be produced over a large area by encapsulating chemical vapor deposition (CVD) SLG in hBN,⁵⁴ large-area multipixel architectures at terahertz frequencies are feasible.

Single-pixel, RT broadband GFET detectors with $\text{NEP} \sim 80 \text{ pW Hz}^{-1/2}$ ³⁶ or $\tau \sim 0.1 \text{ ns}$ have been already reported.^{28,29,55} However, in both refs 28 and 29, the PD ultrafast and broadband response was associated with a quite poor $\text{NEP} > 1 \text{ mW Hz}^{-1/2}$ in ref 28 and $> 8 \text{ nW Hz}^{-1/2}$ in ref 29. These NEP are larger than those required for a practical exploitation of

terahertz RT PDs, especially for imaging, high-resolution spectroscopy and near-field microscopy, where $\text{NEP} < 1 \text{ nW Hz}^{-1/2}$ is preferable.⁶ This motivates the effort to devise SLG PDs combining fast τ ($\sim 1 \text{ ns}$), broadband operation (0.1–10 THz), large (> 3 orders of magnitude) dynamic range, and low ($< 1 \text{ nW Hz}^{-1/2}$) NEP.

In ref 36, a PTE SLG PD was reported with $\text{NEP} < 100 \text{ pW Hz}^{-1/2}$, $\tau \sim 40 \text{ ns}$, a 3 orders of magnitude dynamic range, and operating over a 0.3–4 THz bandwidth. This employed a dual-gated narrow gap (100 nm) dipolar antenna, which, while creating a p-n junction in the SLG channel, concentrates the terahertz field at the junction, where the photoresponse arises.³⁶ However, the $\sim 40 \text{ ns}$ response time (set-up limited) still hinders the application in pulse characterization or high repetition-rate detection.

Here, we increase the speed (electronic bandwidth) and dynamic range of RT SLG PDs, exploiting a much simpler architecture than ref 36, relying on the on-chip patterning of a broadband bow-tie antenna ($\delta\omega/\omega_0 > 20\%$ ⁵⁶) to couple terahertz radiation to a sub-wavelength hBN-SLG-hBN heterostructure with $\mu \sim 53000 \text{ cm}^2 \text{ V}^{-1} \text{ s}^{-1}$. By exploiting both PW and PTE mechanisms we get a low-noise ($\text{NEP} \sim 160 \text{ pW Hz}^{-1/2}$) RT terahertz PD with a 4 orders of magnitude dynamic range and $\tau \sim 3 \text{ ns}$, i.e., 1 order of magnitude faster than any other low NEP ($< 10^{-9} \text{ W Hz}^{-1/2}$) LM based terahertz PD operating at RT reported so far, to the best of our knowledge. A SLG is encapsulated within hBN, forming a clean hBN-SLG-hBN heterostructure.⁵⁷ hBN and SLG flakes are prepared by micromechanical exfoliation⁵⁸ on intrinsic Si +285 nm SiO₂ wafers. The flakes are then picked up sequentially (top hBN, SLG, bottom hBN) with poly(dimethylsiloxane) (PDMS) and polycarbonate (PC) stamps. The stack is then released at 180 °C on the final Si/SiO₂ wafer. This T is higher than the glass transition T of PC ($\sim 150 \text{ }^\circ\text{C}$ ⁵⁹), enabling a better control during transfer thanks to the decreased viscosity of PC.^{54,57} Blisters of trapped contaminants at the interface between hBN and SLG become mobile at this T ^{54,56} and can be pushed along the LMH until they reach an edge, leaving the interfaces contaminant-free.

Once the LMH is placed on the substrate, the FET channel is defined by dry etching, leaving the edge of the SLG channel exposed.^{40,57} The channel has a rectangular shape with length $L_C = 5.4 \mu\text{m}$ and width $W_C = 0.8 \mu\text{m}$ (Figure 1a). One-dimensional edge contacts are then realized by electron beam lithography (EBL) followed by metal deposition (Cr/Au, 10/100 nm). The source (S) and drain (D) electrodes are asymmetrically shaped to favor the required asymmetry for which either PTE or PW or their combination take place within the SLG channel (Figure 1a).³⁴ Before defining the top-gate (G) electrode, a thin oxide layer (Al₂O₃, 10 nm) is deposited via atomic layer deposition (ALD). This prevents leakage current between G and the SLG through the edges of the channel itself. The G contact, covering a length $L_G = 5 \mu\text{m}$ over the SLG channel, is then patterned by EBL and finalized by metal deposition (Cr/Au, 10/100 nm). Similar to the S electrode, the G contact is shaped as the branch of a planar bow-tie antenna, with radius $r_b = 21 \mu\text{m}$ and flare angle 90° (Figure 1a).

The antenna dimensions are chosen following electromagnetic simulations with Comsol Multiphysics (see Supporting Information S1 for further details): a 3 THz radiation, matching the frequency of a terahertz quantum cascade laser (QCL), impinges on the GFET on Si/SiO₂ integrated within a

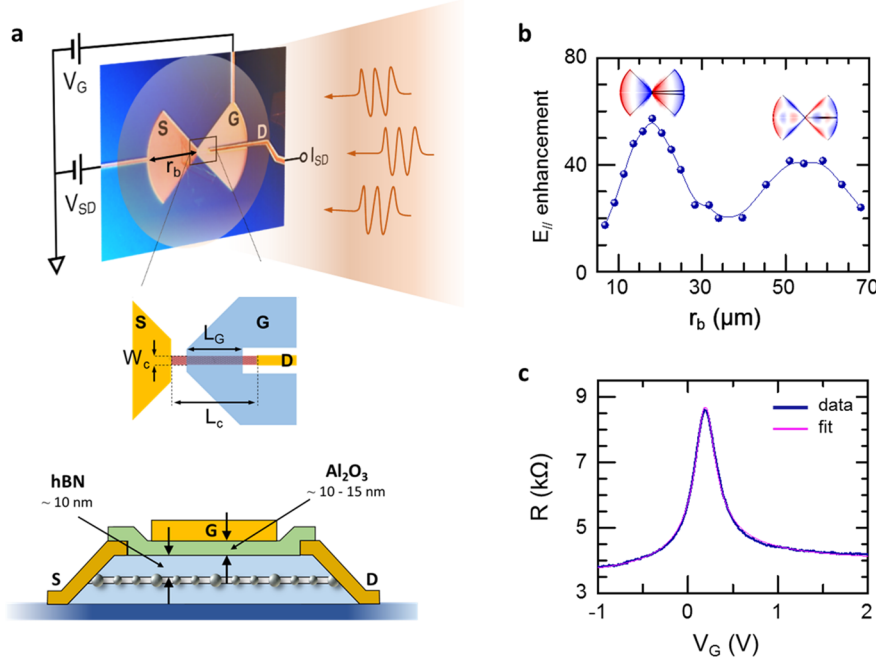


Figure 1. PD layout. (a, bottom) Schematic of PD active area. SLG is encapsulated between two flakes of hBN (bottom 30 nm, top 10 nm). The heterostructure is capped by \sim 10–15 nm Al_2O_3 after edge-contact fabrication.⁴⁰ (a, top) Detector layout. The GFET is embedded in a planar bow-tie antenna (radius $r_b = 21 \mu\text{m}$). The inset shows the main geometrical parameters of the GFET: channel width ($W_c = 0.8 \mu\text{m}$), channel length ($L_c = 5.4 \mu\text{m}$), gate length ($L_G = 5 \mu\text{m}$). (b) Antenna simulations showing the enhancement of the *in-plane* component of the electric field E_{\parallel} at the position of the GFET due to the presence of the antenna, plotted as a function of r_b , for an impinging frequency of 3 THz. (inset) Maps of the out-of-plane component of the electric field for $r_b = 20 \mu\text{m}$ and $r_b = 52 \mu\text{m}$, showing $\lambda/2$ and $3\lambda/2$ resonances. (c) RT two-terminal resistance as a function of top-gate voltage (V_G) from which μ is extracted.

planar bow-tie antenna, whose radius r_b is changed in discrete steps from 6 to 69 μm . Figure 1b plots the simulated enhancement of the in-plane electric field component (E_{\parallel}) provided by the antenna as a function of r_b , with respect to the case where the hBN-SLG-hBN heterostructure is not connected to the antenna. The antenna response shows two maxima at $r_b = 20$ and 52 μm , corresponding to the $\lambda/2$ and $3\lambda/2$ resonances. The inset of Figure 1b shows the out-of-plane component of the electric field on the plane of the antenna. The maximum $|E_{\parallel}|^2$ enhancement is 3500, concentrated in the gap between S and G, creating the required asymmetry³⁴ for the activation of PW and PTE effects.

The devices are then electrically characterized at RT. Figure 1c shows the channel resistance (R), extrapolated by probing the source-drain current (I_{SD}) as a function of top-gate voltage (V_G), while keeping the source-drain voltage $V_{SD} = 2$ mV. The CNP is at $V_G = 0.2$ V. The $R(V_G)$ plot can be used to extract the field effect mobility (μ_{FE}), the residual carrier density (n_0), and the contact resistance (R_0), by fitting R with⁶⁰ $R = R_0 + (L_c/W_c)(1/n_{2d}\mu_{FE})$, where n_{2d} is the gate-dependent charge density, given by⁶⁰ $n_{2d} = [n_0^2 + (C_{Ga}/e(V_G - CNP))^2]^{1/2}$. Here, C_{Ga} is the gate-to-channel capacitance per unit area ($C_{Ga} = 0.2 \mu\text{F cm}^{-2}$), and CNP is used as fixed parameter for the fitting function. We get μ_{FE} (holes) $\sim 41\,000 \pm 800 \text{ cm}^2 \text{ V}^{-1} \text{ s}^{-1}$, μ_{FE} (electrons) $\sim 53\,000 \pm 400 \text{ cm}^2 \text{ V}^{-1} \text{ s}^{-1}$, $n_0 \sim 1.52 \pm 0.01 \times 10^{11} \text{ cm}^{-2}$, $R_0 \sim 3.3 \pm 0.01 \text{ k}\Omega$, and $4.0 \pm 0.01 \text{ k}\Omega$ for hole and electron doping, respectively. These μ are consistent with those of ref 57, and they are the highest reported in any terahertz GFET, to the best of our knowledge.

The GFET is then optically tested using a single-plasmon 2.8 THz QCL, operating at a heat sink temperature $T = 30$ K in a tabletop Stirling cryostat (model Ricor K535). The QCL is

driven in pulsed mode (pulse width 1.6 μs ; repetition rate 40 kHz). The average QCL output power is progressively varied from a few nanowatts to 820 μW , at the corresponding maximum lattice $T = 170$ K (estimated assuming a substrate thermal resistance $\sim 20 \text{ K/W}$ ⁶¹). The 30° divergent terahertz beam is collimated and focused by using two picarin (tsupurica) lenses with focal lengths of 25 and 50 mm (Figure 2a). The resulting Gaussian beam at the focal point has a waist of $\sim 120 \mu\text{m}$. The average optical intensity is increased to a maximum of $\sim 2 \text{ W/cm}^2$. The SLG PD is then mounted onto a roto-translation stage, to move it over the focal plane and modify the relative angle (α in Figure 2a) between the bow-tie antenna axis and the vertically polarized terahertz electric field.

Optical measurements are then performed at RT and at liquid nitrogen T (77 K). The sample is electrically connected as follows: the S electrode is grounded, the G contact is connected to a dc voltage generator (Keithley 2400), and the generated photovoltage signal Δu is measured at the D electrode, connected to a lock-in amplifier (Stanford Research 830, reference/modulation frequency $f_{ref} = 1.334 \text{ kHz}$) through a voltage preamplifier (FEMTO HVA200, gain 100, bandwidth 200 MHz). For the 77 K measurements, the sample is mounted on the cold unit of a gas-refrigerated cryostat (QMC, TK 1800), and the terahertz beam reaches the PD through a 2 mm polymeric window (TPX, transmission $76 \pm 2\%$ at 3 THz). Δu is then estimated from the photovoltage recorded with the lock-in V_{LI} , as $\Delta u = 2.2 \times V_{LI}/\eta$,³² where η is the voltage preamplifier gain coefficient.

Figure 2b shows the map of $|\Delta u|$ (log scale) at RT on the focal plane (xy in Figure 2a) of the terahertz beam, for an impinging average power of $\sim 100 \mu\text{W}$. The GFET has a signal-to-noise ratio (SNR) $> 10^3$ at the optimal $V_G = 0.36$ V.

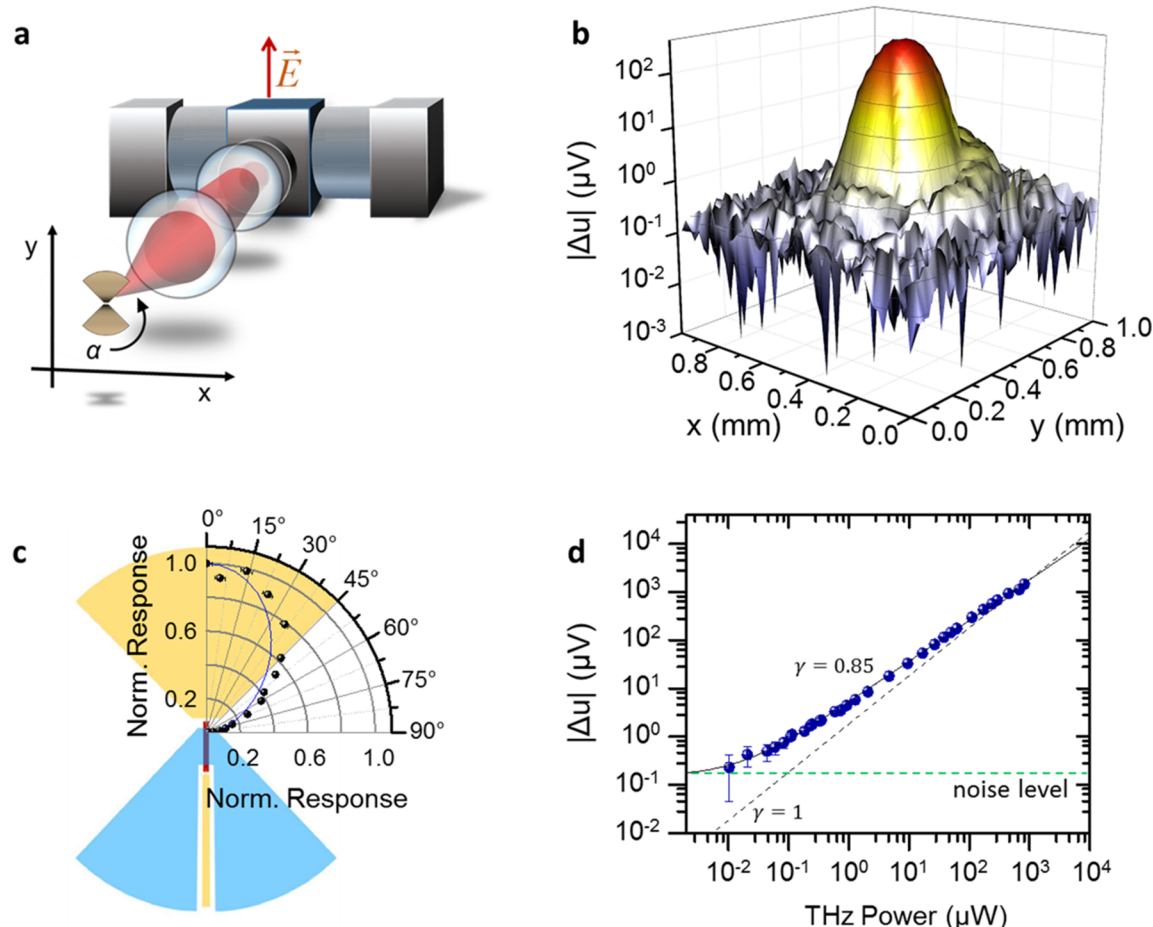


Figure 2. Optical characterization. (a) Schematic of the terahertz experiment: a 2.8 THz QCL is focused on the GFET, whose position (xy plane) and orientation with respect to the laser polarization (angle α) can be controlled. (b) 1×1 mm $|\Delta u|$ map for an impinging power $\sim 100 \mu\text{W}$. The map is obtained by scanning the detector position on the focal xy plane and recording the measured photovoltage when $V_G = 0.36$ V. The ratio between Δu measured at the center ($x = 0.5$ mm, $y = 0.5$ mm) and Δu measured outside the terahertz beam is more than 3 orders of magnitude. (c) Polar plot of the detected signal as a function of α , ranging from 0° (antenna axis parallel to the light polarization) to 90° (antenna axis perpendicular to the light polarization). Black dots: experimental data. Solid blue line: simulation. (d) Absolute value of the photovoltage plotted as a function of the incident power in log–log scale ($V_G = 0.36$ V). The solid line is a fit to the data using $|\Delta u(P)| \sim a_0 + P^\gamma$, where a_0 is the experimental noise floor, and the exponent $\gamma = 0.85$. The dashed black line is for $\gamma = 1$. The error bars are the root-mean-square deviations of the measured $|\Delta u|$.

To verify the polarization selectivity of our antenna geometry,⁵⁶ we measure the THz photoresponse as a function of angle α between antenna axis and THz beam polarization. The photoresponse (Figure 2c) reaches its maximum when the antenna axis is parallel to the polarization and decreases when α is increased from 0° to 90° . The experimental data (black dots) are in good agreement with simulations (solid blue line).

An important figure of merit for a terahertz PD is the dynamic range,^{32,36} i.e., the range of impinging optical power that the PD is capable to sense. To determine it, we vary in regular steps the average output power of the QCL from 0 to $820 \mu\text{W}$ (Figure 2d, and Supporting Information Figure S2). The GFET detects a minimum power ~ 90 nW and a maximum power $\sim 820 \mu\text{W}$. The dependence of the response with respect to power is almost linear over more than 3 orders of magnitude (setup limited), following a power law $|\Delta u| \sim P^\gamma$ with $\gamma = 0.85 \pm 0.007$ (the fit to the data is reported in Figure 2d, black solid line). This quasi-linear dependence of the terahertz photoresponse is expected for both PW and PTE-based PD operating in the *weak-heating* regime;^{36,47} i.e., when the thermal gradient along the GFET channel is smaller than

the heat sink T : $\Delta T \ll 300$ K.³⁵ The small deviation from the linear ($\gamma = 1$) power dependence can be ascribed to the temperature dependence ($\sim T^{-1}$) of the graphene thermal conductivity at RT.⁴⁸

To identify the dominant physical mechanism governing the photodetection process, the PD response is then recorded as a function of V_G at 77 and 300 K. The responsivity R_v is evaluated by normalizing the photovoltage Δu with respect to the optical power impinging on the detector: $R_v = \Delta u / P \times A_{\text{spot}} / A_{\text{diff}}$ ³³ where P is the total terahertz power, A_{spot} is the beam spot area, and A_{diff} is the diffraction-limited area, calculated as $\lambda^2 / 4$,^{32,33} as shown in Figure 3a (left vertical axis). At RT a maximum $|R_v| = 49 \text{ V W}^{-1}$ is found for $V_G = 0.36$ V. At 77 K, $|R_v|$ reaches $\sim 180 \text{ V W}^{-1}$. Both at 300 and 77 K, the R_v plot as a function of V_G shows a double sign switch. Unlike a purely or a dominant overdamped PW (resistive self-mixing) regime, we do not see a single sign change in Δu at the CNP, caused by the sign change in the derivative of the static channel conductance σ in the expression of the PW photovoltage³⁴ $\Delta u_{\text{PW}} \propto -\sigma^{-1} \partial \sigma / \partial V_G$.

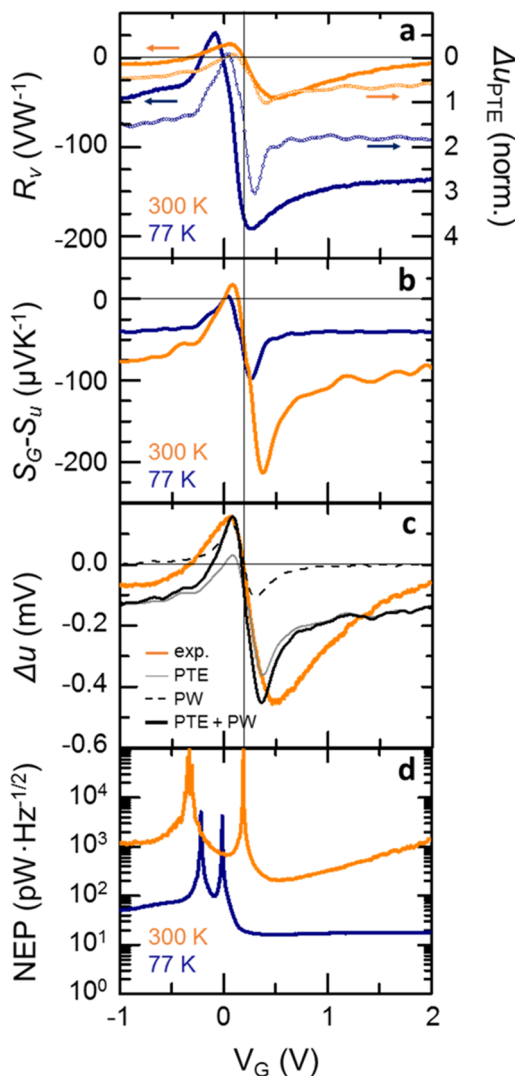


Figure 3. Main figures of merit. (a) Left vertical axis, solid lines: R_v as a function of V_G at RT and 77 K. The double sign switch in the photovoltage is a signature of a dominant PTE. Right vertical axis, dotted lines: estimated Δu_{PTE} , normalized to the maximum at RT. The grey vertical line at $V_G = 0.2$ V indicates the CNP at RT. (b) Estimated difference in the Seebeck coefficient between gated (S_G) and ungated area (S_u) as a function of V_G at RT and at 77 K. (c) Comparison between experimental Δu (measured at $P = 100 \mu\text{W}$) and theoretical PTE, PW, and combined $\Delta u_{\text{PTE}} + \Delta u_{\text{PW}}$ photo-voltages. (d) NEP at 300 and at 77 K evaluated by assuming a Johnson-noise dominated noise spectral density. Minimum NEPs ~ 160 and $18 \text{ pW Hz}^{-1/2}$ are obtained at 300 and 77 K.

The double sign change in the R_v versus V_G plot can be interpreted as the fingerprint of a dominant terahertz-light induced PTE.^{36,43} In this case, the PTE photovoltage is $\Delta u_{\text{PTE}} = (S_G - S_u) \cdot \Delta T$,^{33,34} where S_G is the Seebeck coefficient of the SLG below the G electrode, S_u is the Seebeck coefficient of the ungated regions close to the S and D contacts, and ΔT is the T difference between the S-side and the D-side of the GFET channel. This thermal imbalance is a direct consequence of the asymmetric funneling of terahertz radiation by the bow-tie antenna. The PTE response is given by the diffusion of hot carriers from the hot (S) toward the cold (D) side of the GFET, which results in a measurable electrical signal. S_G can be evaluated from the dc conductivity σ of the GFET, using the Mott equation:³³ $S_{\text{Mott}} = -eL_0T \times \sigma^{-1}(\partial\sigma/\partial V_G) \times (\partial V_G/$

$\partial E_F)$, where $L_0 = (\pi k_B)^2/(3e^2)$ is the Lorenz number, and E_F is the Fermi energy. $\partial V_G/\partial E_F$ can be evaluated from $E_F = \hbar v_F(\pi C_{\text{Ga}}\delta V_G/e)^{1/2}$,⁶² where $\delta V_G = |V_G - V_{\text{CNP}}$. At RT, S_G reaches a maximum $\sim 130 \mu\text{V K}^{-1}$ for $V_G = 0.36 \text{ V}$ (see Supporting Information figure S4). S_u is expected to be $\sim S_G$ when $V_G = 0 \text{ V}$,³³ therefore, it is positive and constant with respect to V_G . $S_G - S_u$ is plotted in Figure 3b for $T = 300 \text{ K}$ and $T = 77 \text{ K}$; in both cases, the two sign changes as a function of V_G are expected. The PTE model can also provide a quantitative interpretation of the increase in R_v at $T = 77 \text{ K}$, with respect to RT. Indeed, ΔT is expected to increase at low T , due to the increased electron cooling length^{43,47} and to the improved electrical characteristics of the GFET³⁵ (details in Supporting Information). The comparison between the calculated Δu_{PTE} at RT and at 77 K is given in Figure 3a (right vertical axis). The maximum PTE response at 77 K is expected to be 3 times larger than the maximum obtained at RT, in quantitative agreement with our measurements.

A more rigorous interpretation can be given by considering the simultaneous interplay of PW and PTE. Figure 3c plots Δu at RT as a function of V_G obtained for an optical power of $\sim 100 \mu\text{W}$ (orange curve), together with the estimated Δu_{PTE} and Δu_{PW} . The solid black line represents the combined theoretical photovoltage $\Delta u_T = \Delta u_{\text{PTE}} + \Delta u_{\text{PW}} = a \times (S_G - S_u) + b\sigma^{-1}(\partial\sigma/\partial V_G)$, where a and b are the fitting parameters. The PW contribution is only relevant close to CNP, whereas PTE dominates at higher carrier densities ($|V_G - V_{\text{CNP}}| > 0.3 \text{ V}$). From the separate evaluation of the two contributions, and the knowledge of a and b , we can estimate ΔT driving the PTE response. By dividing Δu_{PTE} (Figure 3c) by $(S_G - S_u)$ at RT (Figure 3b), we get $\Delta T = \Delta u_{\text{PTE}}/(S_G - S_u) \sim 0.8 \text{ K}$ when the terahertz power is $\sim 100 \mu\text{W}$, which results in a T gradient $\sim 0.2 \text{ K } \mu\text{m}^{-1}$ along the SLG channel. This confirms that the PD operates in the weak-heating regime^{36,47} for all the investigated range of optical terahertz power (0–820 μW).

To assess the PD sensitivity, we evaluate NEP as the ratio between PD noise spectral density (NSD) and R_v . A correct evaluation of NSD is extremely important for a proper estimate of NEP. In our system there are four mechanisms that can have a role in the total noise figure: the Johnson-Nyquist noise (N_J),³⁶ the shot noise,⁶³ the generation-recombination noise,⁶⁴ and the flicker noise (1/f, or telegraph noise).⁶⁵ The first is related to the thermal voltage fluctuations (V_{th}) at the ends of the GFET channel, and its power spectral density is, in turn, related to R and to the heat sink T via¹⁵ $N_J^2 = \langle V_{\text{th}}^2 \rangle = 4k_B T R$. In our case, the N_J contribution to NSD is $\sim 10 \text{ nV Hz}^{-1/2}$ at 300 K and $\sim 4 \text{ nV Hz}^{-1/2}$ at 77 K.

The shot noise of a quantum conductor typically increases under terahertz illumination due to the possibility of photon-assisted shot noise (PASN).⁶³ However, in our T range and under zero bias (no external V_{SD}), the contribution of the shot noise to the total noise figure is expected to be orders of magnitude lower than N_J ,⁶³ therefore, it can be neglected. The same argument applies to the generation-recombination noise, whose amplitude drops below N_J under zero bias and for current densities less than $1 \mu\text{A/mm}$.⁶⁴ The 1/f noise can be neglected with respect to N_J due to the combination of zero-bias detection (no direct current applied) and more than kilohertz modulation frequency ($f_{\text{ref}} = 1.334 \text{ kHz}$).³⁹ Thus, we approximate NSD $\sim N_J$. The NEP is then calculated as $N_J/|R_v|$, and the resulting $\text{NEP}(V_G)$ plots are in Figure 3d for $T = 300$ and 77 K. We get minimum NEP ~ 160 and $18 \text{ pW Hz}^{-1/2}$ for 300 and 77 K, respectively. Notably, the RT NEP is minimum

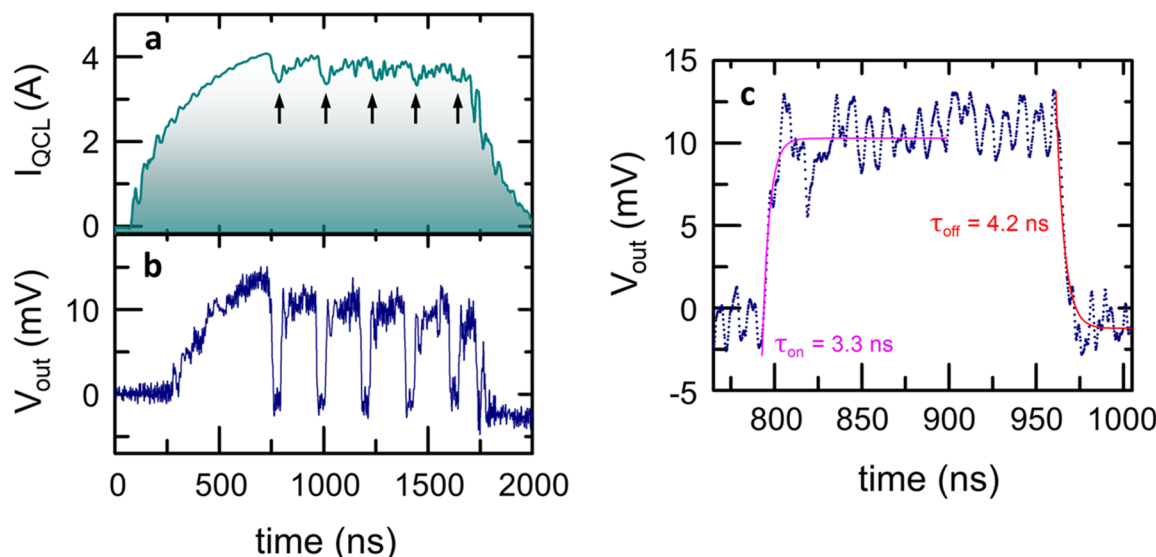


Figure 4. BW evaluation. (a) Driving current of the QCL when the laser is operated in pulse mode: pulse width $1.6 \mu\text{s}$, repetition rate 33 Hz . At high bias ($V_{QCL} > 29 \text{ V}$), the current presents fluctuations corresponding to the *on/off* switching of the laser. (b) Detector signal recorded at $V_G = 0 \text{ V}$, with a 5.0 GS/s oscilloscope. The QCL turns off in an almost regular way (210 ns period). (c) Zooming between two consecutive fluctuations it is possible to retrieve the PD time constants by fitting the waveform with the standard charge-time, discharge-time expressions.³⁶ The estimated rise-time and fall-time are $\tau_{on} \sim 3.3 \text{ ns}$ and $\tau_{off} \sim 4.2 \text{ ns}$, respectively, corresponding to BW $\sim 53 \text{ MHz}$.

when the GFET is n-type, which corresponds to the regime where a *p-n* junction is established between the *S* and *G* electrodes, i.e., the region where the antenna funnels terahertz radiation.

Finally, we evaluate the bandwidth (BW) of our terahertz PD by taking advantage of the employed QCL. When the QCL is driven with high-voltage pulses ($V_{QCL} > 29 \text{ V}$), it enters the so-called negative differential resistance (NDR) regime.⁶⁶ From an electrical point of view, this corresponds to a very unstable high field domain regime, in which the driving current fluctuates randomly under increased applied bias. From an optical point of view, the QCL average output power progressively decreases when increasing the voltage, due to the increased overall temperature of the laser lattice, which, in turn, reduces the population inversion.⁶⁷ In the NDR, the QCL turns off and on many times during a single pulse, as in Figure 4a,b. These abrupt transitions are an intrinsic property of the QCL and are governed by the exchange of energy between electrons, photons, and lattice within the QCL cavity. Thus, the switching from the *off* to the *on* state (and vice versa) is not dictated by external circuitry (power supply and pulse generator) and can be significantly faster than the onset of externally driven pulses (the switching time is expected to be $\sim 1 \text{ ns}$ ⁶⁷).

Figure 4a,b show the time trace of the current flowing through the QCL (I_{QCL}) during a single $1.6 \mu\text{s}$ pulse, recorded with an oscilloscope (resolution 5 GS/s , corresponding to 200 ps) and the corresponding voltage time trace at the output of the GFET, collected at $V_G = 0 \text{ V}$, by using a voltage preamplifier (model A1423, CAEN) with input impedance 50Ω , gain 46 dB and bandwidth 1.2 GHz . The instantaneous power P_i switches on and off in an almost periodic way, with a period $\sim 210 \text{ ns}$. In coincidence with the *off*-state condition, I_{QCL} shows pronounced dips (indicated by vertical arrows in Figure 4a), ascribed to the sudden reduction in the current flow due to the unstable transport arising from the *off-on* turning state within the QCL active region.

The waveform in Figure 4b is used to assess the detector BW. Figure 4c shows a zoom on a single P_i oscillation, from which the rise-time τ_{on} and fall-time τ_{off} are extracted using the fitting functions³⁶ $V_{out} = c_0 + V_{on} \times [1 - \exp(-(t - c_1)/\tau_{on})]$ and $V_{out} = c_2 + V_{off} \times \exp(-(t - c_3)/\tau_{off})$. The fitting parameters c_0 , c_2 and c_1 , c_3 are constants representing voltage offsets and time offsets, respectively; V_{on} and V_{off} are the voltage jumps in the waveform. We obtain a rise (fall) time of $\sim 3.3 \text{ ns}$ (4.2 ns), corresponding to BW $\sim 53 \text{ MHz}$ (38 MHz), where $BW = 1/2\pi\tau$, 1 order of magnitude better than what was observed in ref 36 for a comparable NEP. The GFET itself is expected to show response time of the order of 100 ps .^{28,29,36} The observed rise and fall times are limited by external factors. The first is the detector circuitry, consisting of the cables and preamplifiers (BW $> 1.2 \text{ GHz}$) attached to the device itself, by the chip mount and on-chip components. These are expected to add a parasitic (simulated) capacitance $\sim 1 \text{ pF}$, which, in combination with the $5 \text{ k}\Omega$ resistance of the SLG channel, gives rise to a response time of a few ns, the largest limitation to our rise-time. In addition, the impinging terahertz QCL source is driven by a pulse generator, which has an intrinsic time jitter $\sim 100 \text{ ps}$.⁶⁸ Moreover, in the present setup, the laser can undergo thermal fluctuations of the order of $\pm 1 \text{ K}$ during operation. This effect can smear out the pulses as a consequence of power fluctuations. Our 53 MHz BW is thus a lower limit. This, combined with the $160 \text{ pW/Hz}^{1/2}$ NEP, identifies our device as state-of-the-art among any other uncooled broadband SLG terahertz detectors reported.^{11,29,36}

In conclusion, we demonstrated a record performance GFET PD with a 53 MHz modulation BW, operating at 3 THz . The device operation frequency is set by the coupling scheme, given here by a planar bow-tie antenna, and can be tailored across the whole terahertz range by engineering the antenna design. Changing the size of the antenna would tune its resonance frequency, and changing the type of antenna can narrow or broaden its frequency coverage. We took advantage of the peculiar power instabilities of the QCL source in specific transport regimes, to achieve a response time $\sim 3.3 \text{ ns}$. This,

when combined with our NEP, makes this PD the fastest, low-noise, RT terahertz PD operating at frequencies >1.5 THz. We attribute the BW performance improvement to the high mobility of our hBN-SLG-hBN heterostructure. Further improvements are expected integrating our PDs with on-chip microstrip lines, to reduce the overall circuit capacitance, therefore avoiding possible BW limitations induced by the external FET circuitry. Refinements of the experimental system electronics (e.g., a larger BW, low-noise amplifier) can help to assess the real intrinsic speed limit of our PDs, which is expected to be in the ~10 ps range.³⁶

■ ASSOCIATED CONTENT

Supporting Information

The Supporting Information is available free of charge at <https://pubs.acs.org/doi/10.1021/acs.nanolett.9b05207>.

Bow-tie antenna simulation, quantum cascade laser characterization, description of the photothermoelectric model (PDF)

■ AUTHOR INFORMATION

Corresponding Authors

Leonardo Viti — NEST, Istituto Nanoscienze—CNR, Scuola Normale Superiore, 56127 Pisa, Italy;  orcid.org/0000-0002-4844-2081; Email: leonardo.viti@nano.cnr.it

Miriam S. Vitiello — NEST, Istituto Nanoscienze—CNR, Scuola Normale Superiore, 56127 Pisa, Italy;  orcid.org/0000-0002-4914-0421; Email: miriam.vitiello@sns.it

Authors

David G. Purdie — Cambridge Graphene Centre, University of Cambridge, CB3 0FA Cambridge, U.K.

Antonio Lombardo — Cambridge Graphene Centre, University of Cambridge, CB3 0FA Cambridge, U.K.

Andrea C. Ferrari — Cambridge Graphene Centre, University of Cambridge, CB3 0FA Cambridge, U.K.

Complete contact information is available at:

<https://pubs.acs.org/10.1021/acs.nanolett.9b05207>

Notes

The authors declare no competing financial interest.

■ ACKNOWLEDGMENTS

We acknowledge funding from the ERC Consolidator Grant SPRINT (681379), the EU Graphene Flagship, ERC Grant Hetero2D, and EPSRC Grant Nos. EP/L016087/1, EP/K01711X/1, EP/K017144/1, EP/N010345/1. M.S.V. acknowledges partial support from the second half of the Balzan Prize 2016 in applied photonics delivered to Federico Capasso.

■ REFERENCES

- (1) Kašalynas, I.; Venckevicius, R.; Minkevicius, L.; Sešek, A.; Wahaja, F.; Tamošiūnas, V.; Voisiat, B.; Seliuta, D.; Valušis, G.; Švigelj, A.; Trontelj, J. Spectroscopic Terahertz Imaging at Room Temperature Employing Microbolometer Terahertz Sensors and Its Application to the Study of Carcinoma Tissues. *Sensors* **2016**, *16*, 432.
- (2) Dhillon, S. S.; Vitiello, M. S.; Linfield, E. H.; Davies, A. G.; Hoffmann, M. C.; Booske, J.; Paoloni, C.; Gensch, M.; Weightman, P.; Williams, G. P.; Castro-Camus, E.; Cumming, D. R. S.; Simoens, F.; Escoria-Carranza, I.; Grant, J.; Lucyszyn, S.; Kuwata-Gonokami, M.; Konishi, K.; Koch, M.; Schmuttenmaer, C. A.; Cocker, T. L.; Huber, R.; Markelz, A. G.; Taylor, Z. D.; Wallace, V. P.; Zeitler, J. A.; Sibik, J.; Korter, T. M.; Ellison, B.; Rea, S.; Goldsmith, P.; Cooper, K.

B.; Appleby, R.; Pardo, D.; Huggard, P. G.; Krozer, V.; Shams, H.; Fice, M.; Renaud, C.; Seeds, A.; Stöhr, A.; Naftaly, M.; Ridler, N.; Clarke, R.; Cunningham, J. E.; Johnston, M. B. The 2017 terahertz science and technology roadmap. *J. Phys. D: Appl. Phys.* **2017**, *50*, No. 043001.

(3) Kawase, K.; Ogawa, Y.; Watanabe, Y.; Inoue, H. Non-destructive terahertz imaging of illicit drugs using spectral fingerprints. *Opt. Express* **2003**, *11*, 2549–2554.

(4) Nagai, N.; Kumazawa, R.; Fukasawa, R. Direct evidence of intermolecular vibrations by THz spectroscopy. *Chem. Phys. Lett.* **2005**, *413*, 495–500.

(5) Tonouchi, M. Cutting-edge terahertz technology. *Nat. Photonics* **2007**, *1*, 97–105.

(6) Mittleman, D. M. Twenty years of terahertz imaging. *Opt. Express* **2018**, *26*, 9417–9431.

(7) Koenig, S.; Lopez-Diaz, D.; Antes, J.; Boes, F.; Henneberger, R.; Leuther, A.; Tessmann, A.; Schmogrow, R.; Hillerkuss, D.; Palmer, R.; Zwick, T.; Koos, C.; Freude, W.; Ambacher, O.; Leuthold, J.; Kallfass, I. Wireless sub-THz communication system with high data rate. *Nat. Photonics* **2013**, *7*, 977–981.

(8) Mitrofanov, O.; Viti, L.; Dardanis, E.; Giordano, M. C.; Ercolani, D.; Politano, A.; Sorba, L.; Vitiello, M. S. Near-field terahertz probes with room-temperature nanodetectors for subwavelength resolution imaging. *Sci. Rep.* **2017**, *7*, 44240.

(9) Giordano, M. C.; Viti, L.; Mitrofanov, O.; Vitiello, M. S. Phase-sensitive terahertz imaging using room-temperature near-field nanodetectors. *Optica* **2018**, *5*, 651–657.

(10) Huber, M. A.; Mooshammer, F.; Plankl, M.; Viti, L.; Sandner, F.; Kastner, L. Z.; Frank, T.; Fabian, J.; Vitiello, M. S.; Cocker, T. L.; Huber, R. Femtosecond photo-switching of interface polaritons in black phosphorus heterostructures. *Nat. Nanotechnol.* **2017**, *12*, 207–211.

(11) Sizov, F. Terahertz radiation detectors: the state-of-the-art. *Semicond. Sci. Technol.* **2018**, *33*, 123001.

(12) Simoens, F.; Meilhan, J. Terahertz real-time imaging uncooled array based on antenna- and cavity-coupled bolometers. *Philos. Trans. R. Soc., A* **2014**, *372*, 20130111.

(13) Bulcha, B. T.; Hesler, J. L.; Drakinskiy, V.; Stake, J.; Valavanis, A.; Dean, P.; Li, L. H.; Barker, N. S. Design and Characterization of 1.8–3.2 THz Schottky-Based Harmonic Mixers. *IEEE Trans. Terahertz Sci. Technol.* **2016**, *6*, 737–746.

(14) Boppel, S.; Lisauskas, A.; Mundt, M.; Seliuta, D.; Minkevicius, L.; Kasalynas, I.; Valusis, G.; Mittendorff, M.; Winnerl, S.; Krozer, V.; Roskos, H. G. CMOS Integrated Antenna-Coupled Field-Effect Transistors for the Detection of Radiation From 0.2 to 4.3 THz. *IEEE Trans. Microwave Theory Tech.* **2012**, *60*, 3834–3843.

(15) Viti, L.; Hu, J.; Coquillat, D.; Politano, A.; Knap, W.; Vitiello, M. S. Efficient Terahertz detection in black-phosphorus nanotransistors with selective and controllable plasma-wave, bolometric and thermoelectric response. *Sci. Rep.* **2016**, *6*, 20474.

(16) Daghestani, N.; Parow-Souchon, K.; Pardo, D.; Liu, H.; Brewster, N.; Froley, M.; Cinque, G.; Alderman, B.; Huggard, P. G. Room temperature ultrafast InGaAs Schottky diode based detectors for terahertz spectroscopy. *Infrared Phys. Technol.* **2019**, *99*, 240–247.

(17) Han, R.; Zhang, Y.; Kim, Y.; Kim, D.; et al. 280 and 860 GHz image sensors using Schottky-barrier diodes in 0.13μm digital CMOS. *IEEE J. Solid-State Circuits* **2012**, *48*, 2296–2308.

(18) Zatta, R.; Jain, R.; Pfeiffer, U. Characterization of the noise behavior in lens-integrated CMOS terahertz video cameras. *International Journal of Terahertz Science and Technology* **2018**, *11*, 102–123.

(19) Ikamas, K.; Lisauskas, A.; Boppel, S.; Hu, Q.; Roskos, H. G. Efficient Detection of 3 THz Radiation from Quantum Cascade Laser Using Silicon CMOS Detectors. *J. Infrared, Millimeter, Terahertz Waves* **2017**, *38*, 1183–1188.

(20) Lisauskas, A.; Bauer, M.; Boppel, S.; Mundt, M.; Khamaisi, B.; Socher, E.; Venckevicius, R.; Minkevicius, L.; Kasalynas, I.; Seliuta, D.; Valusis, G.; Krozer, V.; Roskos, H. G. Exploration of Terahertz Imaging with Silicon MOSFETs. *J. Infrared, Millimeter, Terahertz Waves* **2014**, *35*, 63–80.

- (21) Koppens, F. H. L.; Mueller, T.; Avouris, Ph.; Ferrari, A. C.; Vitiello, M. S.; Polini, M. Photodetectors based on graphene, other two-dimensional materials and hybrid systems. *Nat. Nanotechnol.* **2014**, *9*, 780–793.
- (22) Brida, D.; Tomadin, A.; Manzoni, C.; Kim, Y. L.; Lombardo, A.; Milana, S.; Nair, R. R.; Novoselov, K. S.; Ferrari, A. C.; Cerullo, G.; Polini, M. Ultrafast collinear scattering and carrier multiplication in graphene. *Nat. Commun.* **2013**, *4*, 1987.
- (23) Bonaccorso, F.; Lombardo, A.; Hasan, T.; Sun, Z.; Colombo, L.; Ferrari, A. C. Production and processing of graphene and 2d crystals. *Mater. Today* **2012**, *15*, 564–589.
- (24) Ferrari, A. C.; Bonaccorso, F.; Fal'ko, V.; Novoselov, K. S.; Roche, S.; Bøggild, P.; Borini, S.; Koppens, F. H. L.; Palermo, V.; Pugno, N.; Garrido, J. A.; Sordan, R.; Bianco, A.; Ballerini, L.; Prato, M.; Lidorikis, E.; Kivioja, J.; Marinelli, C.; Ryhänen, T.; Morpurgo, A.; Coleman, J. N.; Nicolosi, V.; Colombo, L.; Fert, A.; Garcia-Hernandez, M.; Bachtold, A.; Schneider, G. F.; Guinea, F.; Dekker, C.; Barbone, M.; Sun, Z.; Gallois, C.; Grigorenko, A. N.; Konstantatos, G.; Kis, A.; Katsnelson, M.; Vandersypen, L.; Loiseau, A.; Morandi, V.; Neumaier, D.; Treossi, E.; Pellegrini, V.; Polini, M.; Tredicucci, A.; Williams, G. M.; Hong, B. H.; Ahn, J.-H.; Kim, J. M.; Zirath, H.; van Wees, B. J.; van der Zant, H.; Occhipinti, L.; Di Matteo, A.; Kinloch, I. A.; Seyller, T.; Quesnel, E.; Feng, X.; Teo, K.; Rupesinghe, N.; Hakonen, P.; Neil, S. R. T.; Tannock, Q.; Löfwander, T.; Kinaret, J. Science and technology roadmap for graphene, related two-dimensional crystals, and hybrid systems. *Nanoscale* **2015**, *7*, 4598–4810.
- (25) Romagnoli, M.; Sorianello, V.; Midrio, M.; Koppens, F. H. L.; Huyghebaert, C.; Neumaier, D.; Galli, P.; Templ, W.; D'Errico, A.; Ferrari, A. C. Graphene-based integrated photonics for next-generation datacom and telecom. *Nat. Rev. Mater.* **2018**, *3*, 392–414.
- (26) Vicarelli, L.; Vitiello, M. S.; Coquillat, D.; Lombardo, A.; Ferrari, A. C.; Knap, W.; Polini, M.; Pellegrini, V.; Tredicucci, A. Graphene field-effect transistors as room-temperature terahertz detectors. *Nat. Mater.* **2012**, *11*, 865–871.
- (27) Spirito, D.; Coquillat, D.; De Bonis, S. L.; Lombardo, A.; Bruna, M.; Ferrari, A. C.; Pellegrini, V.; Tredicucci, A.; Knap, W.; Vitiello, M. S. High performance bilayer-graphene terahertz detectors. *Appl. Phys. Lett.* **2014**, *104*, No. 061111.
- (28) Mittendorff, M.; Winnerl, S.; Kamann, J.; Eroms, J.; Weiss, D.; Schneider, H.; Helm, M. Ultrafast graphene-based broadband THz detector. *Appl. Phys. Lett.* **2013**, *103*, No. 021113.
- (29) Cai, X.; Sushkov, A. B.; Suess, R. J.; Jadidi, M. M.; Jenkins, G. S.; Nyakiti, L. O.; Myers-Ward, R. L.; Li, S.; Yan, J.; Gaskell, D. K.; Murphy, T. E.; Drew, H. D.; Fuhrer, M. S. Sensitive room-temperature terahertz detection via the photothermoelectric effect in graphene. *Nat. Nanotechnol.* **2014**, *9*, 814–819.
- (30) Zak, A.; Andersson, M. A.; Bauer, M.; Matukas, J.; Lissauskas, A.; Roskos, H. G.; Stake, J. Antenna-Integrated 0.6 THz FET Direct Detectors Based on CVD Graphene. *Nano Lett.* **2014**, *14*, 5834–5838.
- (31) Bianco, F.; Perenzoni, D.; Convertino, D.; De Bonis, S. L.; Spirito, D.; Perenzoni, M.; Coletti, C.; Vitiello, M. S.; Tredicucci, A. Terahertz detection by epitaxial-graphene field-effect-transistors on silicon carbide. *Appl. Phys. Lett.* **2015**, *107*, 131104.
- (32) Auton, G.; But, D. B.; Zhang, J.; Hill, E.; Coquillat, D.; Consejo, C.; Nouvel, P.; Knap, W.; Varani, L.; Teppe, F.; Torres, J.; Song, A. Terahertz Detection and Imaging Using Graphene Ballistic Rectifiers. *Nano Lett.* **2017**, *17*, 7015–7020.
- (33) Viti, L.; Politano, A.; Zhang, K.; Vitiello, M. S. Thermoelectric terahertz photodetectors based on selenium-doped black phosphorus flakes. *Nanoscale* **2019**, *11*, 1995–2002.
- (34) Bandurin, D. A.; Gayduchenko, I.; Cao, I.; Moskotin, M.; Principi, A.; Grigorieva, I. V.; Goltsman, G.; Fedorov, G.; Svitsov, D. Dual origin of room temperature sub-terahertz photoresponse in graphene field effect transistors. *Appl. Phys. Lett.* **2018**, *112*, 141101.
- (35) Bandurin, D. A.; Svitsov, D.; Gayduchenko, I.; Xu, S. G.; Principi, A.; Moskotin, M.; Tretyakov, I.; Yagodkin, D.; Zhukov, S.; Taniguchi, T.; Watanabe, K.; Grigorieva, I. V.; Polini, M.; Goltsman, G. N.; Geim, A. K.; Fedorov, G. Resonant terahertz detection using graphene plasmons. *Nat. Commun.* **2018**, *9*, 5392.
- (36) Castilla, S.; Terrés, B.; Autore, M.; Viti, L.; Li, J.; Nikitin, A. Y.; Vangelidis, I.; Watanabe, K.; Taniguchi, T.; Lidorikis, E.; Vitiello, M. S.; Hillenbrand, R.; Tielrooij, K.-J.; Koppens, F. H. L. Fast and Sensitive Terahertz Detection Using an Antenna-Integrated Graphene pn Junction. *Nano Lett.* **2019**, *19*, 2765–2773.
- (37) Dyakonov, M.; Shur, M. Detection, mixing, and frequency multiplication of terahertz radiation by two-dimensional electronic fluid. *IEEE Trans. Electron Devices* **1996**, *43*, 3.
- (38) Muraviev, A. V.; Rumyantsev, S. L.; Liu, G.; Balandin, A. A.; Knap, W.; Shur, M. S. Plasmonic and bolometric terahertz detection by graphene field-effect transistor. *Appl. Phys. Lett.* **2013**, *103*, 181114.
- (39) Preu, S.; Kim, S.; Verma, R.; Burke, P. G.; Sherwin, M. S.; Gossard, A. C. An improved model for non-resonant terahertz detection in field-effect transistors. *J. Appl. Phys.* **2012**, *111*, No. 024502.
- (40) Wang, L.; Meric, I.; Huang, P. Y.; Gao, Q.; Gao, Q.; Tran, H.; Taniguchi, T.; Watanabe, K.; Campos, L. M.; Muller, D. A.; Guo, J.; Kim, P.; Hone, J.; Shepard, K. L.; Dean, C. R. One-Dimensional Electrical Contact to a Two-Dimensional Material. *Science* **2013**, *342*, 614–617.
- (41) Giubileo, F.; Di Bartolomeo, A. The role of contact resistance in graphene field-effect devices. *Prog. Surf. Sci.* **2017**, *92*, 143–175.
- (42) Kachorovskii, V. Y.; Shur, M. S. Field effect transistor as ultrafast detector of modulated terahertz radiation. *Solid-State Electron.* **2008**, *52*, 182–185.
- (43) Song, J. C. W.; Rudner, M. S.; Marcus, C. M.; Levitov, L. S. Hot Carrier Transport and Photocurrent Response in Graphene. *Nano Lett.* **2011**, *11*, 4688–4692.
- (44) Nair, R. R.; Blake, P.; Grigorenko, A. N.; Novoselov, K. S.; Booth, T. J.; Stauber, T.; Peres, N. M. R.; Geim, A. K. Fine Structure Constant Defines Visual Transparency of Graphene. *Science* **2008**, *320*, 1308.
- (45) Viljas, J. K.; Heikkilä, T. T. Electron-phonon heat transfer in monolayer and bilayer graphene. *Phys. Rev. B: Condens. Matter Mater. Phys.* **2010**, *81*, 245404.
- (46) Tomadin, A.; Brida, D.; Cerullo, G.; Ferrari, A. C.; Polini, M. Nonequilibrium dynamics of photoexcited electrons in graphene: collinear scattering, Auger processes, and the impact of screening. *Phys. Rev. B: Condens. Matter Mater. Phys.* **2013**, *88*, No. 035430.
- (47) Tielrooij, K.-J.; Hesp, N. C. H.; Principi, A.; Lundeberg, M. B.; Pogna, E. A. A.; Banszerus, L.; Mics, Z.; Massicotte, M.; Schmidt, P.; Davydovskaya, D.; Purdie, D. G.; Goykhman, I.; Soavi, G.; Lombardo, A.; Watanabe, K.; Taniguchi, T.; Bonn, M.; Turchinovich, D.; Stampfer, C.; Ferrari, A. C.; Cerullo, G.; Polini, M.; Koppens, F. H. L. Out-of-plane heat transfer in van der Waals stacks through electron–hyperbolic phonon coupling. *Nat. Nanotechnol.* **2018**, *13*, 41.
- (48) Pop, E.; Varshney, V.; Roy, A. K. Thermal properties of graphene: Fundamentals and applications. *MRS Bull.* **2012**, *37*, 1273–1281.
- (49) Soavi, G.; Wang, G.; Rostami, H.; Purdie, D. G.; De Fazio, D.; Ma, T.; Luo, B.; Wang, J.; Ott, A. K.; Yoon, D.; Bourelle, S. A.; Muench, J. E.; Goykhman, I.; Dal Conte, S.; Celebrano, M.; Tomadin, A.; Polini, M.; Cerullo, G.; Ferrari, A. C. Broadband, electrically tunable third-harmonic generation in graphene. *Nat. Nanotechnol.* **2018**, *13*, 583–588.
- (50) Tielrooij, K. J.; Piatkowski, L.; Massicotte, M.; Woessner, A.; Ma, Q.; Lee, Y.; Myhro, K. S.; Lau, C. N.; Jarillo-Herrero, P.; van Hulst, N. F.; Koppens, F. H. L. Generation of photovoltage in graphene on a femtosecond timescale through efficient carrier heating. *Nat. Nanotechnol.* **2015**, *10*, 437–443.
- (51) Wei, P.; Bao, W. Z.; Pu, Y.; Lau, C. N.; Shi, J. Anomalous Thermoelectric Transport of Dirac Particles in Graphene. *Phys. Rev. Lett.* **2009**, *102*, 166808.
- (52) Lazzeri, M.; Piscanec, S.; Mauri, F.; Ferrari, A. C.; Robertson, J. Electron Transport and Hot Phonons in Carbon Nanotubes. *Phys. Rev. Lett.* **2005**, *95*, 236802.

(53) Lazzeri, M.; Piscanec, S.; Mauri, F.; Ferrari, A. C.; Robertson, J. Phonon linewidths and electron-phonon coupling in graphite and nanotubes. *Phys. Rev. B: Condens. Matter Mater. Phys.* **2006**, *73*, 155426.

(54) De Fazio, D.; Purdie, D. G.; Ott, A. K.; Braeuninger-Weimer, P.; Khodkov, T.; Goossens, S.; Taniguchi, T.; Watanabe, K.; Livreri, P.; Koppens, F. H. L.; Hofmann, S.; Goykhman, I.; Ferrari, A. C.; Lombardo, A. High-Mobility, Wet-Transferred Graphene Grown by Chemical Vapor Deposition. *ACS Nano* **2019**, *13*, 8926–8935.

(55) Generalov, A.; Andersson, M. A.; Yang, X.; Vorobiev, A.; Stake, J. A heterodyne graphene FET detector at 400 GHz. *International Conf. on Infrared, Millimeter, and Terahertz Waves, IRMMW-THz 2017*, 8067234.

(56) Lepeshov, S. I.; Gorodetsky, A.; Krasnok, A. E.; Rafailov, E. U.; Belov, P. A. Enhancement of Terahertz Photoconductive Antennas and Photomixers Operation by Optical Nanoantennas. *Laser Photonics Rev.* **2017**, *11*, 1600199.

(57) Purdie, D. G.; Pugno, N. M.; Taniguchi, T.; Watanabe, K.; Ferrari, A. C.; Lombardo, A. Cleaning interfaces in layered materials heterostructures. *Nat. Commun.* **2018**, *9*, 5387.

(58) Novoselov, K. S.; Jiang, D.; Schedin, F.; Booth, T. J.; Khotkevich, V. V.; Morozov, S. V.; Geim, A. K. Two-dimensional atomic crystals. *Proc. Natl. Acad. Sci. U. S. A.* **2005**, *102*, 10451–10453.

(59) Fan, C. F.; Cagin, T.; Shi, W.; Smith, K. A. Local chain dynamics of a model polycarbonate near glass transition temperature: A molecular dynamics simulation. *Macromol. Theory Simul.* **1997**, *6*, 83–102.

(60) Kim, S.; Nah, J.; Jo, I.; Shahrjerdi, D.; Colombo, L.; Yao, Z.; Tutuc, E.; Banerjee, S. K. Realization of a high mobility dual-gated graphene field-effect transistor with Al₂O₃ dielectric. *Appl. Phys. Lett.* **2009**, *94*, No. 062107.

(61) Vitiello, M. S.; Scamarcio, G.; Spagnolo, V.; Williams, B. S.; Kumar, S.; Hu, Q.; Reno, J. L. Measurement of subband electronic temperatures and population inversion in THz quantum-cascade lasers. *Appl. Phys. Lett.* **2005**, *86*, 111115.

(62) Ghahari, F.; Xie, H.-Y.; Taniguchi, T.; Watanabe, K.; Foster, M. S.; Kim, P. Enhanced Thermoelectric Power in Graphene: Violation of the Mott Relation by Inelastic Scattering. *Phys. Rev. Lett.* **2016**, *116*, 136802.

(63) Parmentier, F. D.; Serkovic-Loli, L. N.; Roulleau, P.; Glattli, D. C. Photon-Assisted Shot Noise in Graphene in the Terahertz Range. *Phys. Rev. Lett.* **2016**, *116*, 227401.

(64) Sokolov, V. N.; Kochelap, V. A.; Kim, K. W. Generation-recombination noise in bipolar graphene. *J. Appl. Phys.* **2011**, *110*, No. 044327.

(65) Balandin, A. A. Low-frequency 1/f noise in graphene devices. *Nat. Nanotechnol.* **2013**, *8*, 549–555.

(66) Castellano, F.; Li, L.; Linfield, E. H.; Davies, A. G.; Vitiello, M. S. Frequency and amplitude modulation of ultra-compact terahertz quantum cascade lasers using an integrated avalanche diode oscillator. *Sci. Rep.* **2016**, *6*, 25053.

(67) Kundu, I.; Wang, F.; Qi, X.; Nong, H.; Dean, P.; Freeman, J. R.; Valavanis, A.; Agnew, G.; Grier, A. T.; Taimre, T.; Li, L.; Indjin, D.; Mangeney, J.; Tignon, J.; Dhillon, S. S.; Rakic, A. D.; Cunningham, J. E.; Linfield, E. H.; Davies, A. G. Ultrafast switch-on dynamics of frequency-tunable semiconductor lasers. *Nat. Commun.* **2018**, *9*, 3076.

(68) www.Avtechpulse.Com/Catalog/Avr-1-2-3-4_rev17.Pdf.